Nuclear Science and Techniques (2025) 36:174
https://doi.org/10.1007/s41365-025-01758-5

Novel Sn-doped ammonium phosphomolybdate: preparation, characterization and adsorption properties of Cs

He-Zhou Chen[1] · Zhen-Nan Wu[1] · Hong-Ji Sang[1] · Hao Wu[1] · Yan Wu[1] · Yue-Zhou Wei[1]

Received: 16 October 2024 / Revised: 29 November 2024 / Accepted: 9 December 2024 / Published online: 2 July 2025

Abstract

With the development of nuclear power, a significant amount of radioactive waste liquid has been generated, among which cesium posed high radioactivity and a long half-life, which necessitated its removal from waste liquids. In this study, a series of Sn-doped ammonium phosphomolybdate adsorbents were synthesized through chemical co-precipitation for the adsorption of cesium. The incorporation of stannum ions replaced one-third of the inert ammonium ions in ammonium phosphomolybdate, which resulted in an increase in the volumetric charge density between molecules and enhanced the performance of the adsorbent. Transmission electron microscopy, scanning electron microscopy, and energy-dispersive spectroscopy analyses revealed that while the face-centered cubic crystal structure of the material remained unchanged, the morphology of the microparticles transitioned from cubic to spherical. According to the results from X-ray diffraction, Fourier transform infrared spectroscopy, and thermogravimetric analysis, as well as adsorption capacity and stability tests, the adsorbent $SnII_{0.5}SnIV_{0.5}(NH4)_2[P(Mo_3O_{10})_4]$ (add Fe), which exhibited the best performance was selected for further investigation. This included X-ray photoelectron spectroscopy, adsorption selectivity, adsorption–desorption cycles, thermodynamics, isotherms, and kinetics experiments. The results indicated that $SnII_{0.5}SnIV_{0.5}(NH4)_2[P(Mo_3O_{10})_4]$ (add Fe) exhibited excellent selectivity for cesium, with the adsorption process characterized as an exothermic ion exchange reaction, which achieved a saturated adsorption capacity of 115 mg/g and maintained over 85% adsorption efficiency after three cycles. Additionally, density functional theory was used to further analyze the changes in the unit cell dimensions and energy of the material. The results demonstrated that this study successfully developed a novel adsorbent based on the ammonium phosphomolybdate matrix, which was capable of efficiently and rapidly extracting Cs from radioactive waste liquids. This study also provided a new idea for the design and development of inorganic materials.

Keywords Micronano-scale · Hybrid · Co-precipitation · Heteropoly salt · Improved stability

1 Introduction

To tackle the global energy crisis and mitigate environmental pollution, advancements in clean energy technologies have driven continuous progress in the global nuclear power industry [1]. However, the operation of nuclear power plants and the reprocessing of spent nuclear fuel generate substantial amounts of radioactive liquid waste. These wastes contain not only fissile materials such as uranium and plutonium but also significant quantities of fission products such as cesium, strontium, palladium, and technetium, which remain highly radioactive [2, 3]. Ensuring the safe and effective treatment and disposal of these liquid wastes is critical for environmental protection and makes the separation and recovery of radioactive nuclides a pressing global challenge [4]. Cesium-137 is particularly concerning owing to its high radioactivity, significant heat generation, and long half-life [5, 6]. Its chemical properties are similar to those of sodium and potassium, and it mainly exists as cesium ions in aqueous solutions. Cesium exhibits high mobility and bioaccumulation, which enables it to easily enter various environments and eventually accumulate in

This work was supported by the National Natural Science Foundation of China (Nos. 12175143).

✉ Yan Wu
wu_yan@sjtu.edu.cn

[1] School of Nuclear Science and Engineering, Shanghai Jiao Tong University, Shanghai 200240, China

human bones and muscle tissues [7]. This bioaccumulation can lead to inflammatory diseases and cancers in various organs and cause irreversible damage. Cesium-137 recovered from radioactive waste liquids can serve as a gamma radiation source for medical applications [8]. Therefore, it is crucial to remove cesium-137 from radioactive wastewater efficiently and rapidly to enable subsequent treatment, minimize environmental and societal harm, and ultimately benefit humanity.

Over the past few decades, various techniques have been developed for the separation of cesium, including chemical precipitation [9], solvent extraction [10–13], and ion exchange [14–17]. While the precipitation method is well-established, it faces practical challenges, such as difficulties in solid–liquid separation in high-radiation environments. Solvent extraction is currently the most widely used method in the industry; however, it carries risks of radiation-induced degradation of solvents and diluents. This degradation can cause severe equipment corrosion and generate substantial amounts of secondary liquid waste. Ion exchange is an effective partitioning technology owing to its high selectivity, large adsorption capacity, simplicity of equipment, and low cost. Various ion exchangers have been studied, including zeolites [18], heteropoly acids [19, 20], ferrocyanides [21], Prussian blue analogs [22], titanium silicates [23], metal sulfides [24], metal-organic frameworks (MOFs) [25], and covalent organic frameworks (COFs) [26]. Among these, ammonium phosphomolybdate (AMP), an inorganic ion exchanger with a Keggin structure composed of $[P(Mo_3O_{10})_4]_3^-$ and ammonium ions, has garnered significant attention. The basic framework of AMP consists of 12 MoO_6 octahedra, with PO_4^- groups at the center of the crystal structure and ammonium ions occupying the interstitial spaces (Fig. 1) [27, 28]. Cesium adsorption occurs through an ion exchange reaction, where ammonium ions in AMP are replaced by cesium ions. Cesium can then be eluted using a concentrated NH_4Cl solution, which enables its separation and recovery. Furthermore, compared with more expensive adsorbents such as COFs (20.0 USD/g), MOFs (47.2 USD/g), or titanium silicates (12.8 USD/g), AMP is highly economical and costs only 0.40 USD/g as a commercially available reagent.

Studies have demonstrated that synthesizing micronano-scale materials or incorporating metal ions into hybrid materials can significantly enhance their mechanical and adsorption properties [29]. Chattopadhyay et al. developed micronano-zirconium phosphate, which improved both the mechanical properties and cesium separation efficiency in ^{137}Cs–^{137m}Ba mixtures [30–32]. Taher Yousefi et al. incorporated cerium into phosphomolybdate, which resulted in higher distribution coefficients for ions such as Tl^+, Pb_2^+, Th_4^+, U_4^+, and Cs^+ and achieved multinuclide separation and desorption [33]. Currently, the main methods for

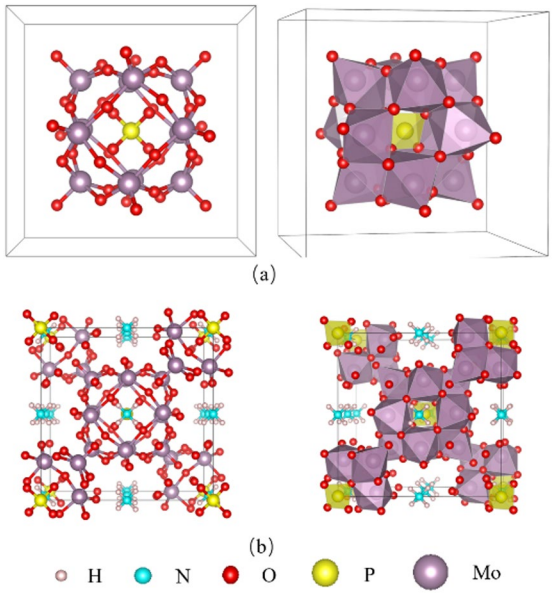

Fig. 1 (Color online) Schematic representation of $[P(Mo_3O_{10})_4]_3^-$ structure (**a**) and crystal structure of AMP (**b**)

preparing micronano-materials include chemical co-precipitation [34, 35], electrochemical deposition [36], vapor deposition [37], and sol–gel methods [38].

Chemical co-precipitation is a simple and cost-effective method for efficiently producing large quantities of micronano-materials. In this study, we synthesized micronano-scale metal-hybridized AMP via the chemical co-precipitation technique. During synthesis, various concentrations of Sn_2^+, Sn_4^+, and Fe_3^+ were introduced into the base material to achieve metal ion hybridization, resulting in the formation of $SnII_xSnIV_y(NH4)_{3-x-y}[P(Mo_3O_{10})_4]$ adsorbents with improved chemical stability and mechanical properties. The incorporation of metal cations with differing sizes and charges into the Keggin structure of AMP, which replaced ammonium ions, altered the material's surface lattice charge and channel size. These modifications in surface net charge and channel dimensions significantly influenced the selectivity and adsorption capacity of the adsorbent. Furthermore, variations in the total surface charge altered the electrostatic forces (attractive or repulsive) between the adsorbent and target nuclides, resulting in a contraction of the unit charge volume. This reduction in unit charge volume enhanced the stability of ion binding and desorption processes, leading to increased adsorption capacity and macroscopic stability [39]. The different valence states of stannum ions selected for this study are expected to uniquely influence material performance. Sn_4^+, with its high charge, is anticipated to significantly enhance the material's properties while Sn_2^+ and Fe_3^+ are expected to induce copolymerization effects during synthesis [40],

promoting the formation of a stable crystal structure in the hybrid material.

Current research on AMP mainly focuses on modifications involving its loading onto various substrates, such as silica or alginate beads. However, this approach may reduce the adsorption capacity of the material due to challenges such as limited loading efficiency. The objective of this study is to directly hybridize multivalent Sn ions into AMP via a chemical co-precipitation method. This approach aims to modify the microstructure of AMP by increasing the charge density per unit volume, which preserves its high adsorption capacity while enhancing its overall adsorption performance. The study involves microscopic characterization and adsorption behavior analysis of the synthesized materials to confirm the successful preparation of Sn-doped AMP and identify the optimal material for further investigation. Additionally, we aim to analyze the fundamental factors contributing to the enhanced performance of the Sn-doped AMP series through experimental characterization and density functional theory (DFT) simulations. These simulations will model changes in energy structures during synthesis and adsorption processes and provide insight into the adsorption mechanism of cesium by Sn-doped AMP.

2 Experimental

2.1 Materials

The chemical reagents used in this study included phosphomolybdic acid ($H_3[P(Mo_3O_{10})_4]$), ammonium chloride (NH_4Cl), tin dichloride ($SnCl_2$), ferric chloride ($FeCl_3$), tin tetrachloride ($SnCl_4$), cesium nitrate ($CsNO_3$), strontium nitrate ($Sr(NO_3)_2$), samarium trinitrate ($Sm(NO_3)_3$), lanthanum nitrate hexahydrate ($La(NO_3)_3 \cdot_6 H_2O$), gadolinium nitrate hexahydrate ($Gd(NO_3)_3 \cdot_6 H_2O$), cerium nitrate ($Ce(NO_3)4$), europium nitrate($Eu(NO_3)_3$), dysprosium nitrate hexahydrate ($Dy(NO_3)_3 \cdot_6 H_2O$), holmium nitrate pentahydrate ($Ho(NO_3)_3 \cdot_5 H_2O$), thulium nitrate pentahydrate ($Tm(NO_3)_3 \cdot_5 H_2O$), ytterbium nitrate ($Yb(NO_3)_3$), lutetium nitrate pentahydrate ($Lu(NO_3)_3 \cdot_5 H_2O$), potassium niobate ($KNbO_3$) and nitric acid (HNO_3). These reagents were procured from Macklin Biochemical Co., Ltd. All of the reagents had a purity of greater than 99.5%, except for $SnCl_4$ (98%) and HNO_3 (65.0%-−68.0%).

2.2 Preparation of the adsorbent

The $SnII_xSnIV_y(NH_4)_{3-x-y}[P(Mo_3O_{10})_4]$ was synthesized via a chemical co-precipitation method, which involved the gradual addition of a hybrid solution containing various components into a soluble solution to ensure uniform mixing and controlled precipitation [40]. First, 100 mL of a 0.05 mol/L phosphomolybdic acid solution was prepared in a beaker. A magnetic stirrer was placed in the beaker, and the solution was stirred at 500 rpm. Appropriate amounts of $SnCl_4$, $FeCl_3$, and $SnCl_2$ hybrid element solutions were then added dropwise to the phosphomolybdic acid solution while maintaining stirring for 30 min. This ensured a complete reaction between the hybrid elements and phosphomolybdic acid. Finally, an adequate amount of NH_4Cl solution was added to enhance the crystallization performance of the material. The solid–liquid mixture was allowed to stand and age for 24 h to facilitate the full development of the microcrystals of the hybrid material. After aging, the mixture was separated using a water aspirator and a Buchner funnel to remove any undeveloped or damaged particles. The material was then washed with deionized water and centrifuged to remove insoluble impurities. Finally, the centrifuged material was dried in a constant-temperature vacuum oven. The resulting adsorbent materials contained various hybrid elements and different hybrid contents. Specific data for each formulation are presented in Table 1, and undried samples are shown in Fig. 2 (In this study, x and y represent the number of ammonium ions replaced in each AMP).

Table 1 Formulations of dopetion

$SnII_xSnIV_y(NH_4)_{3-x-y}[P(Mo_3O_{10})_4]$			
Sample NO	x	y	Whether to add Fe
1	1	0	No
2	0	1	No
3	0.5	0.5	No
4	0.5	0.5	Yes
5	0.2	0.2	Yes
6	0.15	0.15	Yes
7	0.1	0.1	Yes
8	0.4	0	No
9	0	0.4	No
10	0.2	0.2	No

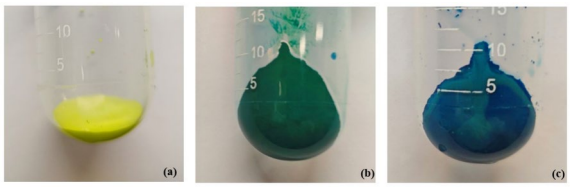

Fig. 2 (Color online) Synthesis products: AMP (**a**), $SnIV_1(NH_4)_2[P(Mo_3O_{10})_4]$(**b**) and $SnII_{0.5}SnIV_{0.5}(NH_4)_2[P(Mo_3O_{10})_4]$(**c**)

2.3 Characterization

The surface morphology was examined using a scanning electron microscope (HITACHI, SU 8600, Japan) and a transmission electron microscope (JEOL, JEM-2100F, Japan). The composition and content of the adsorbent before and after adsorption were analyzed using an energy-dispersive spectroscope (FEI, NOVA NanoSEM 230, America). The unit cell size of the adsorbent was determined using a multifunctional X-ray diffractometer (BRUKER-AXS, D8 ADVANCE Da Vinci, German). The functional groups of the adsorbent were characterized using a Fourier transform infrared spectroscope (THERMO FISHER, Nicolet 6700, America). The thermal decomposition of the adsorbent was evaluated using a thermogravimetric analyzer (Perkin Elmer, TGA8000, America). The valence states and proportions of the main elements were investigated using an X-ray photoelectron spectroscope (AXIS Ultra-DLD, Shimadzu, Japan).

2.4 Adsorption experiments

Batch experiments were conducted to investigate the adsorption capacity and characteristics of the synthesized adsorbents for metal ions. First, the adsorption capacity for Cs and the stability of various materials were examined. The optimal hybrid material was then selected for studying the multi-ion adsorption selectivity. Additionally, the changes in isotherm models at different temperatures for this material were analyzed. Finally, the kinetics of various adsorbents were studied to assess the impact of hybridization on their adsorption rates. A specified amount of adsorbent was added to a glass bottle, followed by the experimental solution (with varying metal ion compositions and concentrations). The bottle was sealed and placed in a pre-set temperature-controlled shaking bath for oscillation. After ensuring complete adsorption (except for kinetic tests), the bottle was removed. The mixture was then filtered to separate the solid from the liquid, and the concentration of target radionuclides in the solution was measured. Unless otherwise specified, the experimental conditions were: V/m=100 cm^3/g, $T = 25°C$, pH=7. The concentrations of Cs and other metal ions were measured using an atomic absorption spectroscopy (Shimadzu, AA-660, Japan) and inductively coupled plasma atomic emission spectroscope (Shimadzu, ICPS-7510, Japan).

2.5 DFT calculations

DFT is a powerful tool for accurately calculating and predicting the electronic properties of crystal structures. DFT avoids the need to solve complex multibody Schrödinger equations by assuming that the energy of the system can be expressed as a function of electron density, which significantly reduces computational load and saves time. In this study, DFT was employed to analyze the adsorption process and mechanism of the hybrid adsorbent for Cs. All of the calculations were performed using the Vienna *Ab Initio* simulation package (VASP 6.2) with plane-wave spin-polarized periodic DFT methods. The projector augmented wave method was used to describe electron–ion interactions and electron exchange and correlation energies were treated using the Perdew-Burke-Ernzerhof generalized gradient approximation function. A cutoff energy of 500 eV, was applied, and the gamma grid was used for Brillouin zone sampling. First, the AMP model was optimized [42], with a force convergence threshold set to less than 0.05 eV/Å. Subsequently, the single-point energies of the system were calculated, with total energy convergence set to less than 10^{-6} eV.

3 Results and discussion

3.1 SEM TEM and EDS

The microstructure of AMP and the $SnII_xSnIV_y(NH_4)_{3-x-y}[P(Mo_3O_{10})_4]$ series was initially examined via scanning electron microscopy (SEM). According to the SEM results, the synthesized AMP predominantly exhibited a cubic structure (Fig. 3a1), with most particles displaying surface defects that impair the mechanical properties of the material. After hybridizing with Sn(IV) alone (Fig. 3a2), the increase in unit volume charge was smaller, and owing to the absence of Fe, complete particles did not form because of the lack of copolymerization effects. Therefore, further investigation of this material will not be pursued. When Sn(IV) and Sn(II) were added simultaneously but without Fe (Fig. 3a3), due to a smaller increase in unit volume charge and the absence of Fe, no complete particles were formed due to the lack of copolymerization effects. Subsequent experiments will not involve further investigation of this material. With the simultaneous addition of Sn(IV) and Sn(II) but without Fe (Fig. 3a4), the material exhibited reduced defects, and the microscopic particles transitioned from a cubic to a spherical structure under the high unit volume charge. Finally, when Fe was added alongside Sn(IV) and Sn(II) ($SnII_{0.5}SnIV_{0.5}(NH_4)_2[P(Mo_3O_{10})_4]$ with Fe) (Fig. 3a5), the copolymerization effect between Sn(II) and Fe(III) enhanced the crystallinity of the material, which resulted in well-formed spherical particles with intact surfaces and significantly improved mechanical properties. After adsorption of cesium ions, the microscopic spheres of $SnII_{0.5}SnIV_{0.5}(NH_4)_2[P(Mo_3O_{10})_4]$ with Fe (Fig. 3a6) showed no significant changes, which indicated that the material retained its stable fundamental structure throughout the adsorption process.

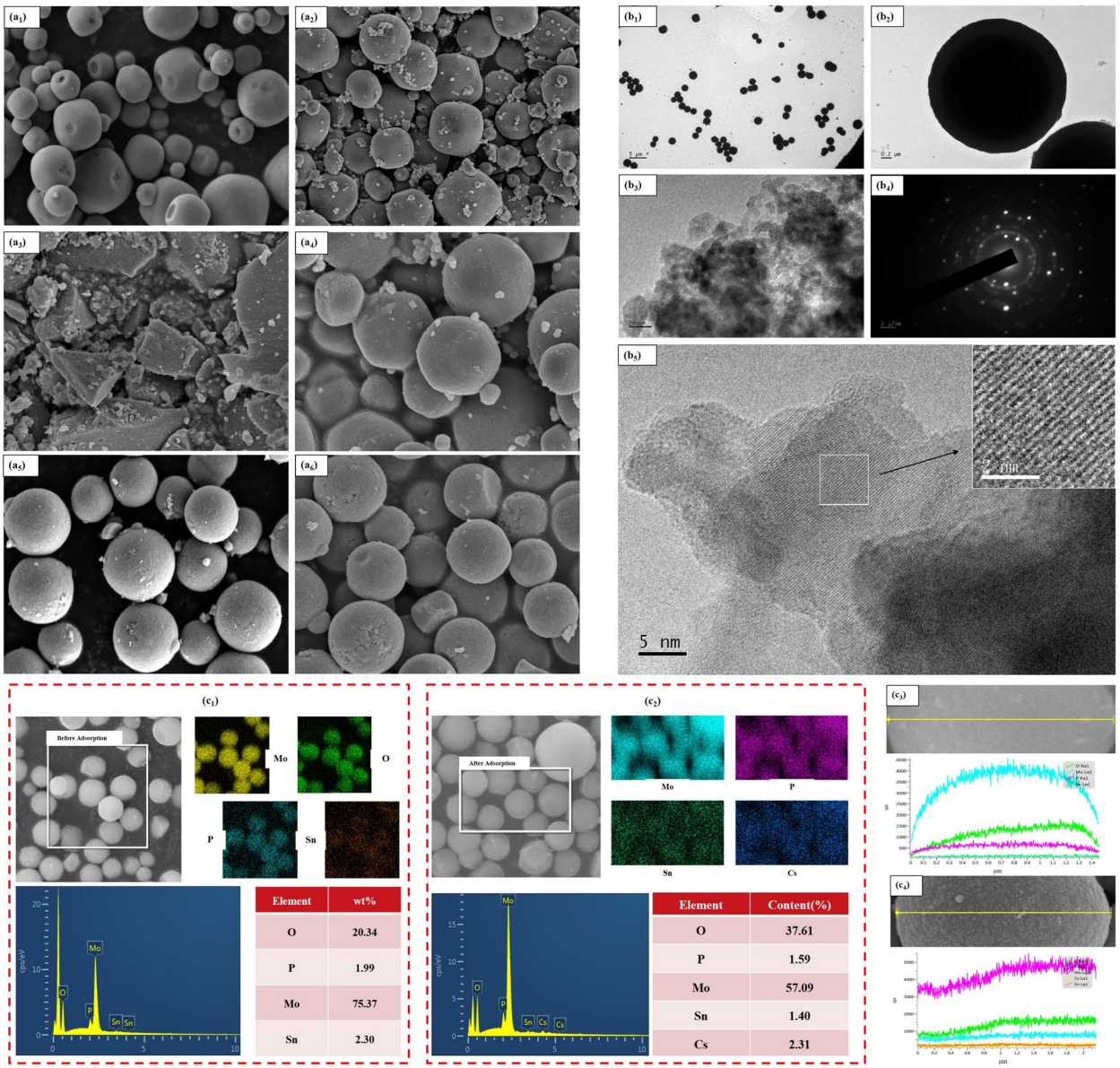

Fig. 3 (Color online) SEM, TEM and EDS results of AMP and Sn-doped-AMP (**a**1–**a**6 SEM images, **b**1–**b**5 TEM images and **c**1-**c**4 EDS results)

Further, the $SnII_{0.5}SnIV_{0.5}(NH_4)_2[P(Mo_3O_{10})_4]$ (add Fe) hybrid material, which featured spherical microparticles, was further analyzed via a transmission electron microscopy (TEM). The TEM images reveal distinct lattice fringes with no noticeable disruptions or displacements, and the consistent spacing between parallel fringes confirms a typical face-centered cubic unit cell structure. The lattice spacing within the unit cell was uniformly distributed. The lattice spacing of the sample was determined to be 2.55 Å by measuring and averaging the spacing between multiple sets of parallel fringes (Fig. 3b5). Figure 3b4 displays uniform reflection rings produced by the numerous brightened nanoscale grains of $SnII_{0.5}SnIV_{0.5}(NH_4)_2[P(Mo_3O_{10})_4]$ (add Fe), as observed through selected area electron diffraction.

Electron dispersive spectroscopy (EDS) analysis was conducted on $SnII_{0.5}SnIV_{0.5}(NH_4)_2[P(Mo_3O_{10})_4]$ (add Fe) to examine the elemental composition and proportions before and after adsorption. Surface scanning results (Fig. 3c1 and c2)confirmed the presence of Sn both before and after adsorption, while Cs is detected only post-adsorption. These findings suggested that Sn was successfully hybridized into AMP and that the hybridized adsorbent retained its Cs adsorption capacity. In addition, there was no significant change in the Sn content or energy relative to Mo, which indicated that Sn does not directly react with Cs. Line scan

results (Fig. 3c3 and c4) revealed a good overlap of characteristic peaks for Sn and Cs after adsorption and demonstrated that both elements coexisted in a similar form within the material and that a substitution reaction with ammonium ions occurred [43].

3.2 The Sn-doped-AMP

To identify the optimal hybrid adsorbent, a series of microstructural characterizations and batch adsorption experiments were performed on the Sn-doped AMP.

The crystalline structure of AMP and Sn-doped AMP was analyzed using X-ray diffraction (XRD). The relative intensity and distinct peaks confirmed the good crystallinity of the products (Fig. 4a1). For the Sn-doped AMP, the diffraction peaks shifted to the right compared with those of AMP in the order of Sn(II) >Sn(II) + Sn(IV) > Sn(IV). This shift indicated a reduction in lattice constants, which was attributed to the smaller ionic radii of the hybrid elements compared with ammonium ions (ionic radii: NH_4^+, 0.143 nm; Sn_2^+, 0.093 nm; Sn_4^+, 0.069 nm). Additionally, the higher ionic charge of the hybrid elements further reduced the unit cell volume. The formation of Sn(II)-O-Sn(IV) bonds might also contribute to the peak shift and the contraction of the unit cell volume. As shown in Fig. 4a1, the sample containing added Fe exhibited sharper diffraction peaks, which highlighted improved crystallinity due to the copolymerization effect of Fe(III) and Sn(II).

Furthermore, the effect of various hybrid concentrations (NH_4^+ substitution ratios) on the structure of the Sn-doped AMP was analyzed. Figure 4a2 demonstrates that within a specific range of hybrid concentrations, the peak intensity of the samples increased with rising concentrations, which indicated that the hybrid elements promote crystal growth. According to the width and intensity of the diffraction peaks, the Scherrer equation was applied to calculate the average grain size of the samples [44]:

$$D = \frac{0.89\lambda}{\beta \cos\theta} \quad (1)$$

where D represents the average grain size, λ denoted the wavelength of the incident X-rays, β referred to the full width at half maximum of the diffraction peak, and θ indicated the diffraction angle.

According to the Scherrer equation, the AMP samples exhibited an average particle size of 73.5 nm, while the hybridized samples showed a reduced average particle size ranging from 55 nm to 65 nm. This indicates a noticeable decrease in particle size due to hybridization.

Second, Fig. 4b shows the Fourier Transform Infrared Spectroscopy (FT-IR) analysis results for AMP and the Sn-doped-AMP samples. Both AMP and Sn-doped-AMP exhibited characteristic peaks at 1063 cm^{-1} (O=P-OH groups), 965 cm^{-1} (Mo-O absorption), 868 cm^{-1} (Mo-O-Mo absorption), and 765 cm^{-1} (antisymmetric stretching vibration of PO_4^{3-}), which confirmed that the Keggin structure of the hybridized samples remained intact. Some samples display a bending vibration peak of H-O-H at 1630 cm^{-1} and a stretching vibration peak of H-O-H at 3210 cm^{-1} attributed to insufficient drying and the presence of crystallization water. Additionally, the N-H bending vibration peak at 1385 cm^{-1} confirmed the presence of ammonium ions in the samples. These ammonium ions contributed to enhanced material crystallinity. Notably, after adsorption, the intensity of the N-H bending vibration peak decreased relative to the characteristic O=P-OH group peak and the Keggin structure peak of $[PMo_{12}O_40]^{3-}$ in the infrared spectra. This decrease indicated a reduction in ammonium ion content, which suggested their involvement in the adsorption process. In the infrared spectra of the Sn-doped-AMP samples, a characteristic peak for Sn at 2976 cm^{-1} was observed. This peak remained detectable after adsorption, which confirmed the successful hybridization and stability of metal ions within the material as they did not detach during adsorption. Lastly, although the functional groups of the samples were similar, the Sn-doped-AMP exhibited a shift toward lower wavenumbers, which were attributed to structural changes induced by hybridization and are consistent with the XRD results.

Third, Fig. 4c and Table 2 present the thermogravimetric analysis (TGA) results for AMP and the Sn-doped-AMP, which showed that all four materials underwent three stages of decomposition. The first stage involved weight loss due to the release of crystalline water from the material. The second stage corresponded to the decomposition of ammonium ions into NH_3 gas. In this stage, AMP exhibited a weight loss of 2.58%, while the Sn-doped-AMP showed a weight loss of approximately 1.6%, which aligned with theoretical values of 2.79% and 1.76%, respectively. The final weight loss stage resulted from the decomposition of phosphomolybdic acid into phosphorus and molybdenum compounds, leading to the destruction of the Keggin structure and loss of cesium adsorption capability [45]. Despite the similar pyrolysis processes, the thermal stability of the materials improved following hybridization. Notably, the $SnII_1(NH_4)_2[P(Mo_3O_{10})_4]$ sample began releasing ammonia only at 765°C, whereas AMP initiated ammonia release at 710°C. The improved thermal stability is attributed to the enhanced interaction forces between the internal components of the molecules after hybridization, resulting in a significant increase in pyrolysis temperature compared to other materials.

Fourth, a comparison of the adsorption capacities of various adsorbents was conducted. Adsorption capacity experiments involved using 50 mg of each hybridized material with a 1200 ppm Cs aqueous solution (Fig. 4d). the main components of the samples from various hybrid

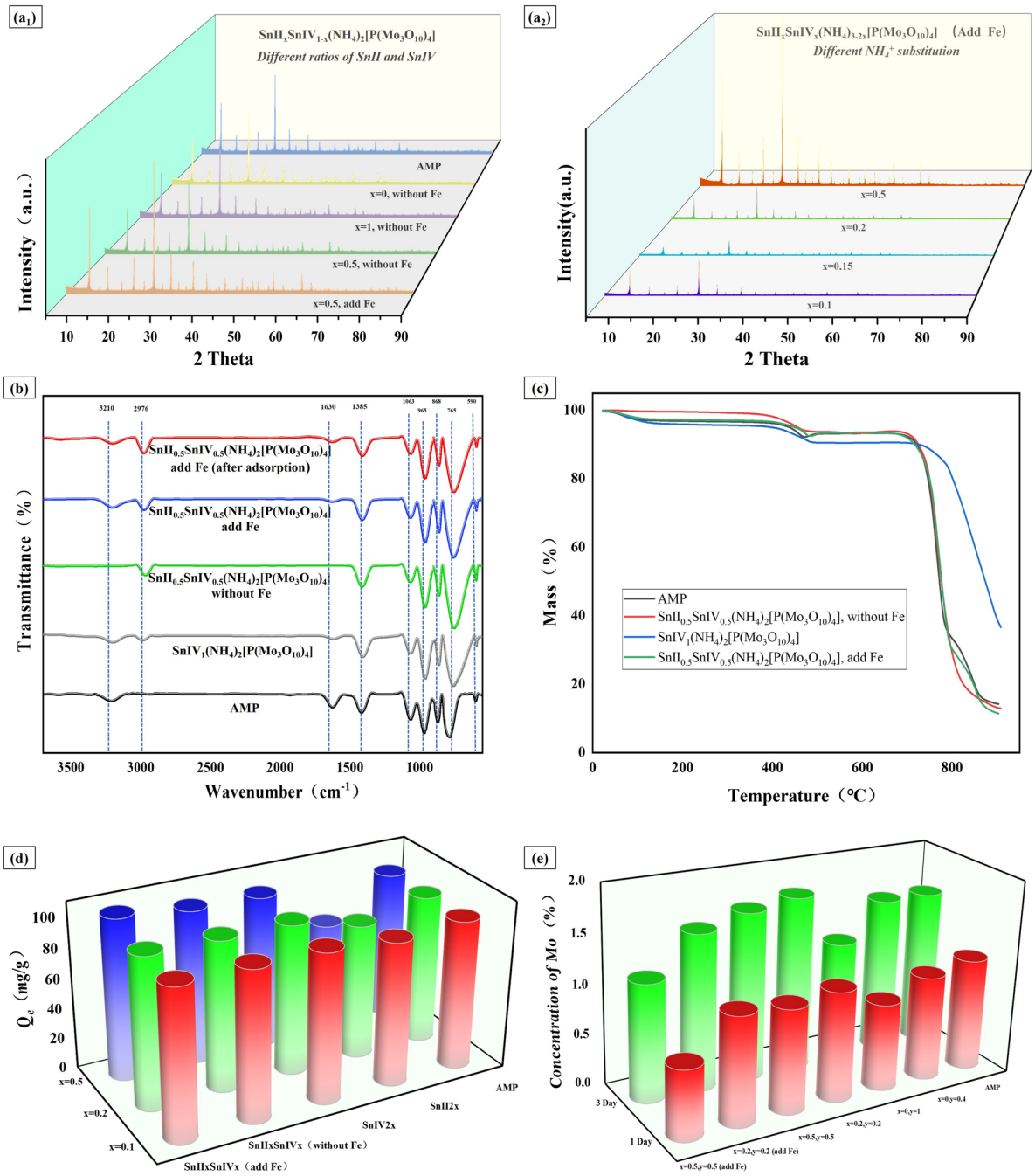

Fig. 4 (Color online) XRD, FT-IR, TGA, adsorption capacity and stability results of AMP and Sn-doped-AMP (**a**1–**a**2 XRD results, **b** FT-IR image, **c** TGA image, **d** adsorption capacity and e stability)

formulations still showed a high degree of similarity to AMP, which resulted in adsorption capacities comparable to those of AMP. However, the adsorption capacity of all materials increased with the doping amount, except for those hybridized with Sn(II) alone. Linking this with the SEM results, it can be inferred that the increase in adsorption capacity is due to the transition of the material's microstructure from cubes to polyhedra and eventually to spheres, which led to an increase in the specific surface area. Compared with AMP, the $SnII_{0.5}SnIV_{0.5}(NH_4)_2[P(Mo_3O_{10})_4]$ (add Fe) exhibited the highest adsorption capacity of 106.8 mg/g, which represented an increase of approximately 10%. In contrast, the decreased adsorption capacity of the Sn(II)-doped AMP could be attributed to the presence of Sn(II) alone, which lacked the high charge of Sn(IV) to enhance material

Table 2 The TGA results of AMP and Sn-doped-AMP

Sample	Pyrolysis stage	Temperature (°C)	Mass loss (%)
AMP	The release of crystalline water	25–465	8.78
	The decomposition of ammonium ions	465–710	2.58
	The decomposition of phosphomolybdic acid	710–930	> 77
$SnII_{0.5}SnIV_{0.5}(NH_4)_2[P(Mo_3O_{10})_4]$ (without Fe)	The release of crystalline water	25–465	8.78
	The decomposition of ammonium ions	465–710	2.58
	The decomposition of phosphomolybdic acid	710–930	> 77
$SnIV_1(NH_4)_2[P(Mo_3O_{10})_4]$	The release of crystalline water	25–465	8.78
	The decomposition of ammonium ions	465–710	2.58
	The decomposition of phosphomolybdic acid	710–930	> 77
$SnII_{0.5}SnIV_{0.5}(NH_4)_2[P(Mo_3O_{10})_4]$ (add Fe)	The release of crystalline water	25–465	8.78
	The decomposition of ammonium ions	465–710	2.58
	The decomposition of phosphomolybdic acid	710–930	> 77

performance. Additionally, it did not form a stable crystal configuration through copolymerization with Fe(III).

Finally, stability is a crucial factor for the practical use of materials. To assess this, chemical stability experiments were conducted on several hybrid materials with good adsorption capacities by immersing the materials in distilled water and measuring the Mo leaching rate at various time intervals.($SnII_{0.5}SnIV_{0.5}(NH_4)_2[P(Mo_3O_{10})_4]$ (add Fe))demonstrated excellent stability, with Mo leaching rates of 0.69% and 1.18% after 1 and 3 days, respectively (Fig. 4e). These values were significantly lower than those of AMP, which indicated that the copolymerization effect of $Sn_2{}^+$ and $Fe_3{}^+$ during synthesis enhanced the crystallization of the hybrid material. Additionally, the high charge and small volume of Sn_4^+ reduced the unit charge volume and further improved the stability of the material. This improvement in stability also reduced the leakage of metal ions during the material's practical application, which was beneficial for environmental protection.

According to the experimental results, the $SnII_{0.5}SnIV_{0.5}(NH_4)_2[P(Mo_3O_{10})_4]$ (add Fe), which retained the effective Keggin structure and exhibited good thermal stability, demonstrated the highest adsorption capacity and excellent chemical stability among the various Sn-doped-AMP materials. Therefore, it was selected as the hybrid material for subsequent in-depth research.

3.3 The $SnII_{0.5}SnIV_{0.5}(NH_4)_2[P(Mo_3O_{10})_4]$ (add Fe) hybridized material

First, X-ray photoelectron spectroscopy (XPS) analysis was conducted to investigate the adsorption mechanism of Cs on $SnII_{0.5}SnIV_{0.5}(NH_4)_2[P(Mo_3O_{10})_4]$ (add Fe). Figure 5a1 shows the full spectrum of $SnII_{0.5}SnIV_{0.5}(NH_4)_2[P(Mo_3O_{10})_4]$ (add Fe) before and after Cs adsorption. Distinct Cs 3d peaks were observed, which confirmed the successful adsorption of Cs onto the hybrid material. Additionally, no Fe-related peaks were detected in the full spectra before or after adsorption. This absence was attributed to the small ionic radius of Fe(III), which might prevent it from forming stable products with the Keggin structure of AMP. Further peak deconvolution of the main elements revealed no significant changes in their binding energies.

Figure 5a2 and a3 displays the high-resolution Mo 3d spectra. Before adsorption, the binding energies for Mo were 233.11 eV, 236.26 eV (Mo^{6+}, as well as 232.19 and 235.27 eV (Mo^{5+}), with corresponding proportions of 51.17%, 35.30% (Mo^{6+}) and 8.00%, 5.52% (Mo^{5+}), respectively. After adsorption, the binding energies shifted to 232.72 eV, 235.87 eV (Mo^{6+}) and 231.53 eV, 234.76 eV (Mo^{5+}), with proportions of 53.27%, 36.72% (Mo^{6+}) and 5.93%, 4.09% (Mo^{5+}), respectively. The binding energies and peak area proportions for the various valence states of Mo showed no significant changes, which indicated that no redox reactions involving Mo occurred during the adsorption process.

Figure 5a4 and a5 presents the high-resolution Sn 3d spectra. Before adsorption, the binding energies for Sn were 487.25 eV and 495.66 eV (Sn^{2+}) and 487.49 eV, 496.10 eV (Sn^{4+}), with proportions of 28.23%, 19.55% (Sn^{2+}) and 31.33%, 20.89% (Sn^{4+}), respectively. After adsorption, the binding energies shifted to 486.85 eV, 495.25 eV (Sn^{2+}) and 487.39 eV, 495.79 eV (Sn^{4+}), with proportions of 23.77%, 16.46% (Sn^{2+}) and 35.69%, 24.08% (Sn^{4+}), respectively. Similar to the Mo results, the binding energies and peak area proportions of the various valence states of Sn showed no significant changes, which confirmed the absence of redox reactions involving Sn during the adsorption process. Combined with the IR spectroscopy results, it can be concluded that the adsorption mechanism of Cs on the $SnII_{0.5}SnIV_{0.5}(NH_4)_2[P(Mo_3O_{10})_4]$ (add Fe) mainly involved an ion-exchange reaction.

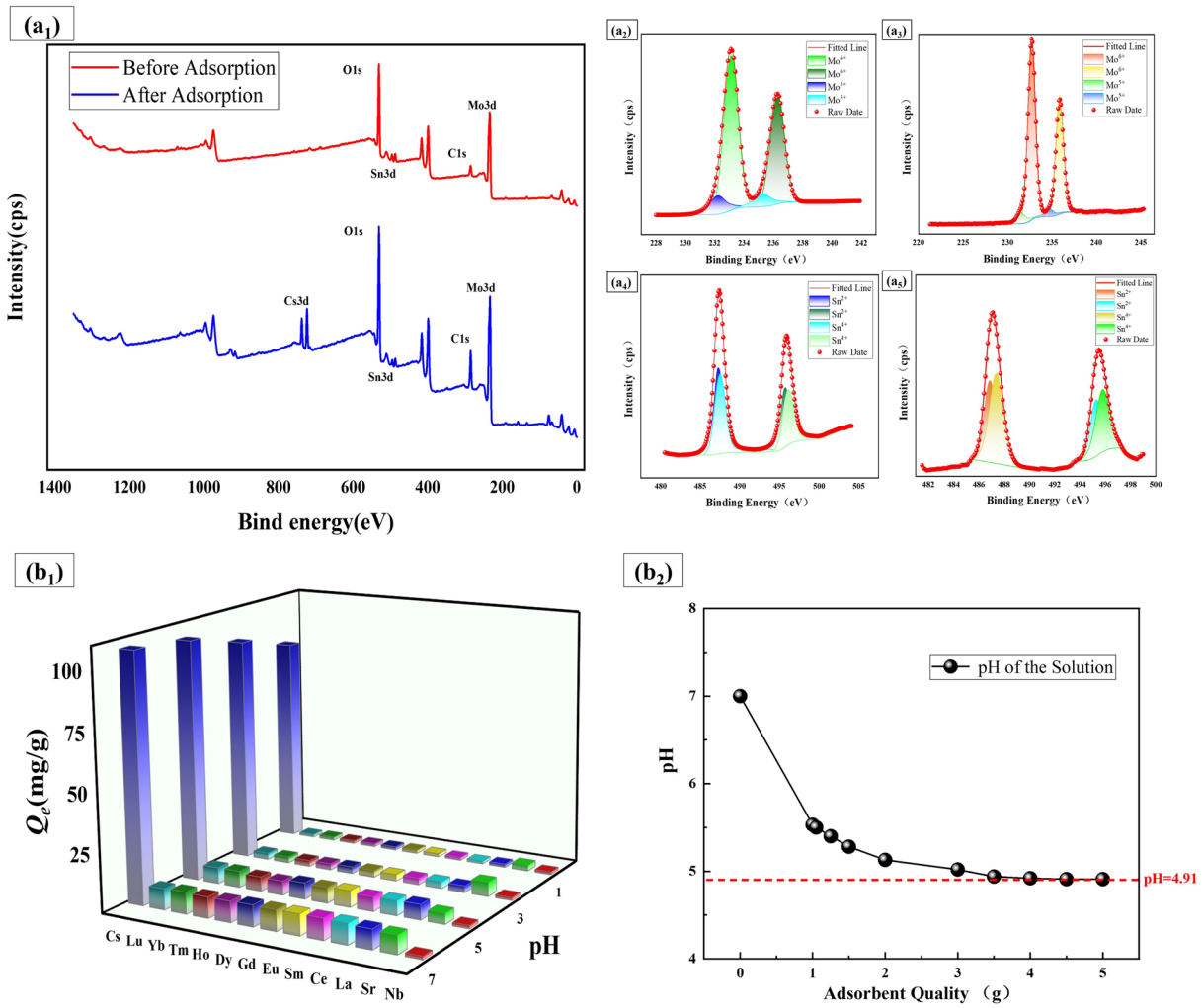

Fig. 5 (Color online) XPS, adsorption selectivity and PZC of $SnII_{0.5}SnIV_{0.5}(NH_4)_2[P(Mo_3O_{10})_4]$ (add Fe) (**a**1–**a**5 XPS results, **b**1 adsorption selectivity, **b**2 the PZC curve)

Second, radioactive wastewater contained various metal ions, which often interfered with each other during industrial processes, leading to a reduced adsorption capacity of the adsorbent for target radionuclides [46]. Therefore, it is essential to assess the adsorption selectivity of $SnII_{0.5}SnIV_{0.5}(NH_4)_2[P(Mo_3O_{10})_4]$ (add Fe). $SnII_{0.5}SnIV_{0.5}(NH_4)_2[P(Mo_3O_{10})_4]$ (add Fe) was introduced to mixed ion solutions at different pH values and adsorption capacity curves for various ions were plotted (Fig. 5b1). In mixed ion solutions at different pH values, $SnII_{0.5}SnIV_{0.5}(NH_4)_2[P(Mo_3O_{10})_4]$ (add Fe) demonstrated a high adsorption capacity for Cs, with almost no adsorption of other metal elements in the solution (e.g., Sr, Eu). This result indicated that $SnII_{0.5}SnIV_{0.5}(NH_4)_2[P(Mo_3O_{10})_4]$ (add Fe) retained good adsorption selectivity for cesium under various conditions. Additionally, as the pH decreased, the adsorption capacity of $SnII_{0.5}SnIV_{0.5}(NH_4)_2[P(Mo_3O_{10})_4]$ (add Fe) decreased, mainly owing to the competition between H^+ and Cs^+ during the adsorption process. The point of zero charge (PZC) pH value of $SnII_{0.5}SnIV_{0.5}(NH_4)_2[P(Mo_3O_{10})_4]$ (add Fe) was measured via the mass titration method [47]. As shown in Fig. 5b2, the PZC of$SnII_{0.5}SnIV_{0.5}(NH_4)_2[P(Mo_3O_{10})_4]$ (add Fe) is 4.91. When the solution pH was lower than 4.91, a large amount of H^+ ions accumulated on the surface of the adsorbent. The high concentrations of H^+ ions could electrostatically interact with metal cations and reduce the adsorption capacity of the material [48, 49].

Third, to evaluate the effect of temperature on the adsorption process, the thermodynamic parameters of the adsorption reaction were calculated using the Van't Hoff equation:

$$\ln K_d = \frac{-\Delta H}{RT} + \frac{\Delta S}{R} \quad (2)$$

$$\Delta G = \Delta H - T\Delta S \tag{3}$$

As shown in Fig. 6a, the (K_d) values at different temperatures were fitted to the Van't Hoff equation, which yielded a correlation coefficient (R^2) of 0.9623. Further analysis of the fitted equation provided the thermodynamic parameters–standard enthalpy (ΔH), standard entropy (ΔS), and Gibbs free energy (ΔG) for this adsorption experiment, as presented in Table 3.

From the table, it can be observed that the ΔH value is negative, which indicated that the reaction is exothermic. The negative ΔS value suggests that the driving force of the reaction decreased with increasing temperature, which means the K_d value decreased as temperature rose [50]. Additionally, calculations revealed that the ΔG values for the adsorption reaction remain negative up to 215.48°C.

Fourth, the adsorption isotherms illustrated the relationship between the amount of adsorbate adsorbed by the adsorbent at equilibrium and the concentration of the target radionuclide in the solution. These isotherms can be used to identify specific adsorption mechanisms and calculate the saturated adsorption capacity of the adsorbent.

The Langmuir model assumes that the adsorption reaction is a monolayer adsorption process with constant adsorption energy. The fitting equation is:

$$Q_e = \frac{Q_m K_L C_e}{1 + K_L C_e}, \tag{4}$$

where Q_e is the adsorption capacity, Q_m is the maximum adsorption capacity, C_e is the equilibrium concentration of Cs in the solution, and K_L is the Langmuir constant.

The Freundlich model assumes that the adsorption occurs on a heterogeneous adsorbent surface with multiple layers of adsorption. The fitting formula is:

$$Q_e = K_F C_e^{\frac{1}{n}}, \tag{5}$$

where K_F is the Freundlich constant, and $1/n$ is the Freundlich isotherm coefficient.

Table 3 The thermodynamic parameters of $SnII_{0.5}SnIV_{0.5}(NH_4)_2[P(Mo_3O_{10})_4]$ (add Fe)

Temperature (K)	ΔH (KJ/mol)	ΔS (KJ/mol · K)	$T\Delta S$ (KJ/mol)	ΔG (KJ/mol)
298	−68.39	−0.14	−41.72	−26.67
303			−42.42	−25.97
308			−43.12	−25.27
313			−43.82	−24.57
318			−44.52	−23.87

The Temkin model accounts for adsorbate-adsorbate interactions and assumes that the adsorption energy decreases linearly as the surface coverage increases. The fitting formula is:

$$Q_e = \frac{RT}{b_T} \ln C_e + \frac{RT}{b_T} \ln K_T, \tag{6}$$

where R is the gas constant, T is the absolute temperature, K_T is the Temkin isotherm equilibrium binding constant, and b_T is the Temkin isotherm constant related to the heat of sorption.

The Dubinin-Radushkevich (D-R) model assumes that the adsorption process follows a porous filling mechanism with a Gaussian distribution of adsorption energies. The fitting equation is:

$$\ln Q_e = \ln Q_m - K_D \varepsilon^2 \tag{7}$$

$$\varepsilon = RT \ln\left(1 + \frac{1}{C_e}\right) \tag{8}$$

$$E = \left(2K_D\right)^{-\frac{1}{2}} \tag{9}$$

The nonlinear Langmuir and Freundlich fitting results for the hybrid materials at different temperatures are shown in Fig. 6b1, with the estimated isotherm parameters listed in Table 4. For all temperature conditions, the Langmuir model consistently provided better fits, with correlation coefficients (R^2) exceeding 0.975. This suggested that the adsorption process of $SnII_{0.5}SnIV_{0.5}(NH_4)_2[P(Mo_3O_{10})_4]$ (add Fe) followed a monolayer adsorption mechanism. According to the Langmuir isotherm model fitting, the maximum adsorption capacities of $SnII_{0.5}SnIV_{0.5}(NH_4)_2[P(Mo_3O_{10})_4]$ (add Fe) at 25 °C, 35 °C, and 45 °C were 115.00 mg/g, 108.78 mg/g, and 102.06 mg/g, respectively. These values indicated that $SnII_{0.5}SnIV_{0.5}(NH_4)_2[P(Mo_3O_{10})_4]$ (add Fe) possessed significant adsorption capacity over a wide temperature range, which demonstrated its effectiveness in purifying Cs from radioactive wastewater. Moreover, the maximum adsorption capacities obtained from the model fit at different temperatures were in close agreement with the experimental results, which further validated the suitability of the Langmuir isotherm model.

However, in some cases, the best-fit model for adsorption materials cannot be determined solely by R^2, which might introduce some ambiguity [51]. The Langmuir isotherm model suggested that monolayer, uniform adsorption dominated under non-competitive equilibrium conditions. In contrast, the Freundlich isotherm model mainly examined the adsorption mechanism through the K_F and $1/n$ values, which helped infer the favorability of metal ion adsorption onto the adsorbent [52]. The Freundlich

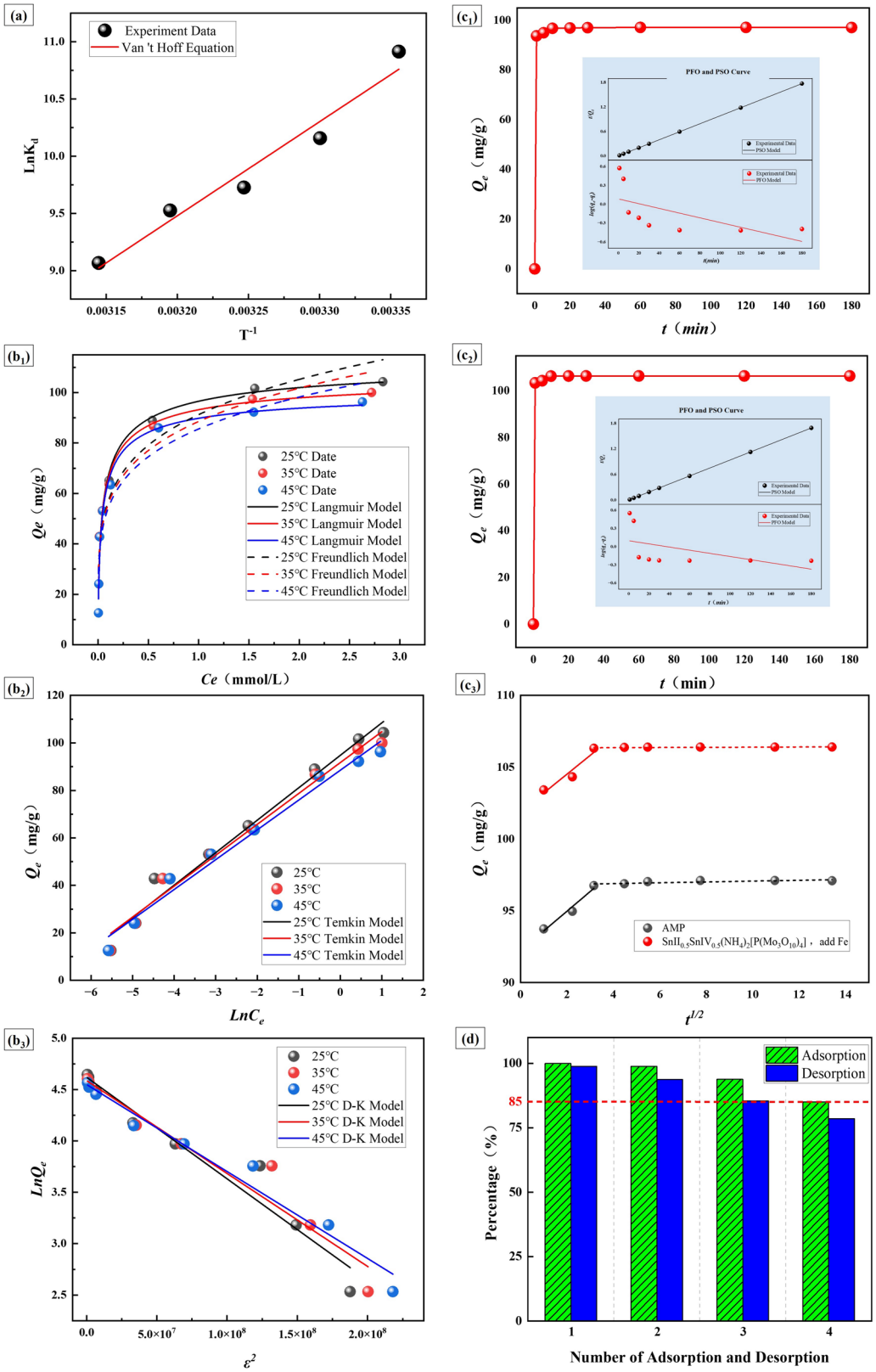

Fig. 6 (Color online) Adsorption performance of $SnII_{0.5}SnIV_{0.5}(NH_4)_2[P(Mo_3O_{10})_4]$ (add Fe) (**a** thermodynamic experiment, **b**1–**b**3 isotherm capacity, **c**1 contact time and fitted curves of AMP, **c**2 contact time and fitted curves of $SnII_{0.5}SnIV_{0.5}(NH_4)_2[P(Mo_3O_{10})_4]$ (add Fe), **c**3 the intraparticle diffusion model, **c** adsorption–desorption

Table 4 The parameters of adsorption isotherms of SnII0.5SnIV0.5$(NH_4)2[P(Mo_3O_{10})_4]$ (add Fe)

Experimental temperature	Isotherm model	Estimated isotherm parameters (H_2O, pH=7)	
25°C	Langmuir	Q_m	115.00
		K_L	5.25
		R^2	0.9777
	Freundlich	K_F	91.27
		$1/n$	0.21
		R^2	0.9240
	Temkin	b_T	184.21
		K_T	1152.64
		R^2	0.9793
	Dubinin-Radushkevich	K	29.71
		E	1297.50
		R^2	0.9477
	Experimental data	Q_m	106.77
35°C	Langmuir	Q_m	108.78
		K_L	6.00
		R^2	0.9751
	Freundlich	K_F	88.56
		$1/n$	0.20
		R^2	0.9180
	Temkin	b_T	196.83
		K_T	1156.36
		R^2	0.9749
	Dubinin-Radushkevich	K	27.46
		E	1350.86
		R^2	0.9441
	Experimental data	Q_m	100.06
45°C	Langmuir	Q_m	102.06
		K_L	7.34
		R^2	0.9860
	Freundlich	K_F	85.59
		$1/n$	0.20
		R^2	0.9199
	Temkin	b_T	210.67
		K_T	1157.69
		R^2	0.9823
	Dubinin-Radushkevich	K	23.23
		E	1468.05
		R^2	0.9731
	Experimental data	Q_m	96.32

model fitting results indicated that the $1/n$ values for $SnII_{0.5}SnIV_{0.5}(NH_4)_2[P(Mo_3O_{10})_4]$ (add Fe) at different temperatures fell within the range of 0.1-10, specifically 0.21 (25°C), 0.20 (35°C), and 0.20 (45°C), which were considered favorable for adsorption.

In the Temkin model(Fig. 6b2), the correlation coefficient (R^2) for $SnII_{0.5}SnIV_{0.5}(NH_4)_2[P(Mo_3O_{10})_4]$ (add Fe) at different temperatures was greater than 0.97, which indicated a high level of accuracy for this model. The value of b_T was greater than 1, which suggested that the reaction was endothermic and aligned with the thermodynamic results [53]. In the D-R model (Fig. 6b3), the average adsorption energy (E) for $SnII_{0.5}SnIV_{0.5}(NH_4)_2[P(Mo_3O_{10})_4]$ (add Fe) was approximately 1000 kJ/mol, which was significantly higher than 8 kJ/mol and indicated that the adsorption of Cs involved the breaking and reorganization of molecular bonds, characteristic of a chemisorption process [54].

Fifth, the surface characteristics of the adsorbent directly influenced the adsorption rate, mainly due to the significant effect of diffusion resistance on ion transport during the adsorption process.

To describe the change in adsorption of the target nuclide over time, we selected the pseudo-first-order (PFO) and pseudo-second-order (PSO) kinetic models, which corresponded to physical and chemical adsorption, respectively.

The PFO kinetic model was based on membrane diffusion theory and a physical adsorption model. The expressions for the nonlinear and linear PFO kinetic models are as follows:

The pseudo-first-order kinetic model is based on the membrane diffusion theory and a physical adsorption model. The expressions for the nonlinear and linear pseudo-first-order kinetic models include the following:

$$q_t = q_e(1 - e^{-k_1 t}) \tag{10}$$

$$\log(q_e - q_t) = \log q_e - \frac{k_1}{2.303} t \tag{11}$$

where k_1 is the adsorption rate constant of the PFO kinetic model, and q_t and q_e are the adsorption capacities of the adsorbent for the target nuclide at time t and equilibrium, respectively.

The PSO kinetic model represents a chemical adsorption process, where electrons are shared or transferred between the adsorbate and the adsorbent. The expressions for the two forms of the PSO kinetic model are as follows:

$$\frac{dq_t}{dt} = k_2(q_e - q_t)^2 \tag{12}$$

$$\frac{t}{q_t} = \frac{1}{k_2 q_e^2} + \frac{t}{q_e} \tag{13}$$

where k_2 is the adsorption rate constant of the PSO kinetic model, and q_t and q_e represent the adsorption capacities of the adsorbent for the target nuclide at time t and equilibrium, respectively.

Figure 6c1, c2 shows the adsorption rates of AMP and $SnII_{0.5}SnIV_{0.5}(NH_4)_2[P(Mo_3O_{10})_4]$ (add Fe), along with the fitted curves for the PFO and PSO models. As observed from the figure, the adsorption of AMP and $SnII_{0.5}SnIV_{0.5}(NH_4)_2[P(Mo_3O_{10})_4]$ (add Fe) achieved uptake ratios of over 96% within 1 min and reached equilibrium quickly. This indicates that, after hybridization, $SnII_{0.5}SnIV_{0.5}(NH_4)_2[P(Mo_3O_{10})_4]$ (add Fe) retains the extremely high adsorption rate of AMP while improving its adsorption capacity. Table 5 presents the parameters of the fitted curves for AMP and the $SnII_{0.5}SnIV_{0.5}(NH_4)_2[P(Mo_3O_{10})_4]$ (add Fe). Both materials were best described by the PSO kinetic model, with correlation coefficients greater than 0.99. This suggested that the adsorption process of the hybrid materials was chemical in nature, which aligned with the XPS measurement results. Additionally, the PSO kinetic parameters of the hybrid materials were similar to those of AMP, which indicated that hybridization did not alter the kinetic properties of the material, which still retained a high adsorption rate. According to the fitting results, the equilibrium adsorption capacities of $SnII_{0.5}SnIV_{0.5}(NH_4)_2[P(Mo_3O_{10})_4]$ (add Fe) under these conditions were in close agreement with the experimentally measured values, which confirmed the accuracy of the model.

Table 5 The parameters of Kinetic models of AMP and $SnII_xSnIV_y(NH_4)_{3-x-y}[P(Mo_3O_{10})_4]$ series

Sample	Kinetic models	Estimated kinetic parameters (25°C H_2O 1500 ppm Cs)	
AMP	PFO Model	k_1	0.0086
		q_e	1.21
		R^2	0.3876
	PSO model	k_2	0.21
		q_e	96.63
		R^2	0.9999
	IPD model Stage 1	k_I	1.37
		C	92.23
		R^2	0.9647
	IPD model Stage 2	k_I	0.029
		C	96.73
		R^2	0.9743
	Experimental data	q_m	97.21
$SnII_{0.5}SnIV^{-}_{0.5}(NH_4)2-[P(Mo_3O_{10})_4]$(add Fe)	PFO Model	k_1	0.0061
		q_e	1.25
		R^2	0.2599
	PSO model	k_2	0.31
		q_e	106.38
		R^2	0.9999
	IPD model Stage 1	k_I	1.31
		C	101.91
		R^2	0.9568
	IPD model Stage 2	k_I	0.0057
		C	106.35
		R^2	0.9372
	Experimental data	q_m	106.82

Furthermore, this study also investigated particle diffusion during the adsorption process of $SnII_{0.5}SnIV_{0.5}(NH_4)_2[P(Mo_3O_{10})_4]$ (add Fe) using the intraparticle diffusion model (IPD). The equation for the intraparticle diffusion model is as follows:

$$q_t = K_I t^{\frac{1}{2}} + C \tag{14}$$

where K_I is the IPD constant and C is the constant associated with the IPD, which is proportional to the boundary layer thickness.

As shown in Fig. 6c3, the adsorption processes of $SnII_{0.5}SnIV_{0.5}(NH_4)_2[P(Mo_3O_{10})_4]$ (add Fe) and AMP for Cs can be mainly divided into two stages. The first stage is the relatively steep surface diffusion stage, during which Cs is rapidly adsorbed onto the surface of $SnII_{0.5}SnIV_{0.5}(NH_4)_2[P(Mo_3O_{10})_4]$ (add Fe). However, it is noteworthy that the curve does not pass through the origin, indicating that internal diffusion is not the sole factor controlling the adsorption process [55]. The second stage is the more gradual internal diffusion stage, where, due to the occupation of a large number of adsorption sites on the surface and within the pores of $SnII_{0.5}SnIV_{0.5}(NH_4)_2[P(Mo_3O_{10})_4]$ (add Fe), the adsorption process transitions to diffusion within the particles, resulting in a significant decrease in the adsorption rate and ultimately reaching equilibrium [56, 57].

Finally, desorption performance and reusability were crucial parameters for evaluating the effectiveness of adsorbents. In this experiment, a 500 ppm Cs solution was used for adsorption, and 3 M NH_4Cl was employed as the desorbent. The adsorption–desorption experiments were conducted at pH 7. After each adsorption, the adsorbent was immersed in 3 M NH_4Cl for desorption, followed by a new adsorption cycle. This process was repeated for a total of four cycles. As shown in Fig. 6d, the desorption rate did not reach 100% after each cycle, leading to a gradual decline in the adsorption efficiency of $SnII_{0.5}SnIV_{0.5}(NH_4)_2[P(Mo_3O_{10})_4]$ (add Fe). However, both the desorption rate in the third cycle and the adsorption rate in the fourth cycle remained above 85%, which indicated that $SnII_{0.5}SnIV_{0.5}(NH_4)_2[P(Mo_3O_{10})_4]$ (add Fe) exhibited good reusability and could meet the demands of practical industrial applications.

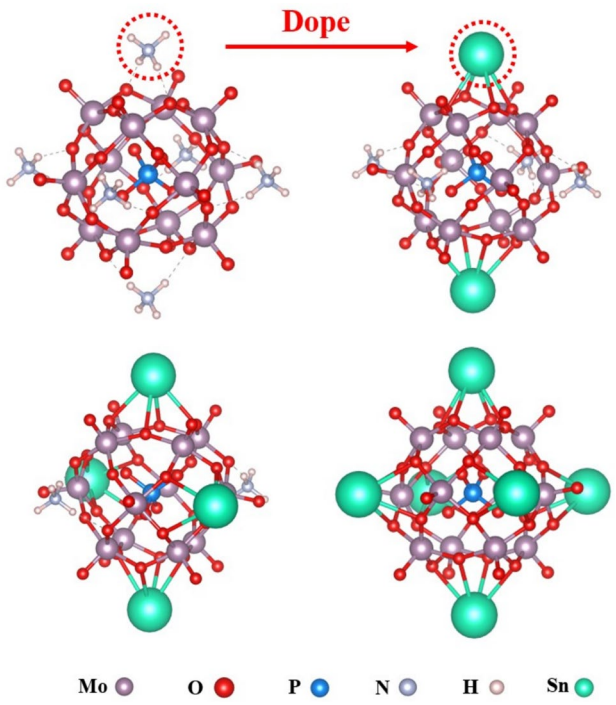

Fig. 7 The different DFT substitution models of AMP and Sn-doped AMP. (Color online)

Table 6 Calculation of cell parameters by DFT

Kind	Number of Sn	*a* (Å)	*b* (Å)	*c* (Å)	*V* (Å^3)
AMP	0	10.93	10.93	10.99	1313.19
AMP-Sn1	1	11.03	10.08	11.07	1230.66
AMP-Sn2	2	10.09	10.09	11.00	1120.05
AMP-Sn3	3	10.22	10.22	10.22	1068.03

3.4 DFT analysis

DFT simulations were performed to model the molecular structure of the synthesized hybrid materials and calculate their energy changes. First, the adsorption process was simulated by systematically replacing ammonium ion sites in AMP with other ions. When Fe atoms were introduced as substitutes, the model results failed to converge, which indicated that Fe could not directly react with AMP. This finding aligned with the microscopic characterization results obtained from EDS and XPS. A series of initial model structures for the hybrid materials were obtained by substituting ammonium ions with Sn atoms (Fig. 7). Table 6 lists the crystal structural parameters of AMP and $SnII_xSnIV_y(NH_4)_{3-x-y}[P(Mo_3O_{10})_4]$ after optimization. Calculations were performed to determine the cell parameters of each material, energy changes during synthesis, and energy changes during the adsorption process. Static calculations were conducted on energy changes to obtain the total free energy changes for each system. The energy calculation formula is as follows:

$$E_{\text{binding}} = E_{\text{free}} - E_{\text{atom}} \tag{15}$$

$$E_{\text{adsorption}} = E_{\text{binding}} + xE_{\text{binding}}(NH_4{}^+) - E_{\text{binding}}(AMP) - xE_{\text{atom}}(Cs)$$

According to the DFT calculation results, when Sn ions replaced ammonium ions, the cell size of the crystals decreased, with the simulation results aligning with experimental findings. Additionally, based on the energy calculation results in Table 7, the substitution of Sn was a spontaneous exothermic reaction. The binding energy was lowest when only one Sn ion was substituted, which indicated that this configuration was the most stable. However, during subsequent adsorption processes, if two ammonium ions were replaced by Sn ions during synthesis, the reaction became endothermic and could not proceed spontaneously. Therefore, it was crucial to strictly control the Sn concentration and the drop rate of the solution during the synthesis of hybrid materials to ensure optimal hybridization conditions. According to previous research conducted by our group, two-thirds of the active ammonium ions in AMP underwent ion exchange reactions [58]. The hybrid material demonstrated optimal adsorption performance when one-third of the ammonium ions were substituted.

Table 7 Calculation of energy by DFT

Kind	Atom energy (eV)	Kind	Free energy (eV)	Binding energy (eV)	Adsorption energy (eV)
Mo	−0.1948	AMP	−505.917	−502.6947	–
O	−0.0180	NH4+	−20.8477	−20.803	–
P	−0.0308	AMP-Sn1	−486.373	−483.187	−1.288
N	−0.01882	AMP-Sn2	−466.537	−463.388	−2.285
H	−0.00637	AMP-Sn1-Cs1	−465.814	−462.601	−0.144
Cs	−0.07209	AMP-Sn1-Cs2	−445.155	−441.914	−0.188
Sn	−0.00728	AMP-Sn2-Cs1	−445.809	−442.633	0.025

This suggested that the non-active ammonium ions in AMP could be replaced by the hybrid element, which enhanced the stability and mechanical properties of the material while maintaining its adsorption capacity.

4 Conclusion

In this study, a series of Sn-doped AMP adsorbents were successfully prepared via the chemical co-precipitation method for the efficient removal of cesium from radioactive waste solutions. Through various characterizations, the best-performing adsorbent, $SnII_{0.5}SnIV_{0.5}(NH_4)_2[P(Mo_3O_{10})_4]$ (add Fe), was selected, and its adsorption mechanisms and performance were further investigated in detail. The $SnII_{0.5}SnIV_{0.5}(NH_4)_2[P(Mo_3O_{10})_4]$ (add Fe) exhibited excellent chemical stability, adsorption selectivity and reusability for Cs. The adsorption of Cs follows a exothermic, monolayer chemisorption process, with a saturated adsorption capacity of 115 mg/g. DFT simulations revealed that following hybridization, Sn replaced an inactive ammonium ion in AMP and enhanced the performance of the remaining two active ammonium ions and hybrid molecules. This process improved both the stability and adsorption performance of the material. This work provides an effective approach for designing high-performance adsorbents for Cs separation. In addition, to meet the requirements property of hybrid material, more stringent synthesis control, such as types of hybridizing agent, reaction rate, aging time and son on is needed.

Author Contributions All authors contributed to the study conception and design. Material preparation, data collection and analysis were performed by He-Zhou Chen, Zhen-Nan Wu and Hong-Ji Sang. The first draft of the manuscript was written by He-Zhou Chen, and all authors commented on previous versions of the manuscript. All authors read and approved the final manuscript.

Data Availability The data that support the findings of this study are openly available in Science Data Bank at https://cstr.cn/31253.11.sciencedb.j00186.00700 and https://doi.org/10.57760/sciencedb.j00186.00700.

Declarations

Conflict of interest The authors declare that they have no Conflict of interest.

References

1. L. Wang, R.X. Gao, H.O. Nam et al., Sustainability-oriented prioritization of nuclear fuel cycle transitions in China: a holistic MCDM framework under uncertainties. Nucl. Sci. Tech. **35**, 158 (2024). https://doi.org/10.1007/s41365-024-01504-3
2. Q. Zou, S. Gu, R.Q. Liu et al., Extraction chromatography-electrodeposition (EC-ED) process to recover palladium from high-level liquid waste. Nucl. Sci. Tech. **28**, 175 (2017). https://doi.org/10.1007/s41365-017-0327-3
3. Z.X. Fang, M. Yu, Y.G. Huang et al., Theoretical analysis of long-lived radioactive waste in pressurized water reactor. Nucl. Sci. Tech. **32**, 72 (2021). https://doi.org/10.1007/s41365-021-00911-0
4. S.C. Zhang, S.Y. Ning, J. Zhou et al., New insight into the adsorption of ruthenium, rhodium, and palladium from nitric acid solution by a silica-polymer adsorbent. Nucl. Sci. Tech. **31**, 34 (2020). https://doi.org/10.1007/s41365-020-0744-6
5. Y.W. Chen, J.L. Wang, Removal of cesium from radioactive wastewater using magnetic chitosan beads cross-linked with glutaraldehyde. Nucl. Sci. Tech. **27**, 43 (2016). https://doi.org/10.1007/s41365-016-0033-6
6. J.R. Liu, Y.D. Xu, W.S. Zhang et al., Solidification performance and mechanism of typical radioactive nuclear waste by geopolymers and geopolymer ceramics: A review. Prog. Nucl. Energ. **169**, 105106 (2024). https://doi.org/10.1016/j.pnucene.2024.105106
7. W. Geng, Y. Liu, D. Wang et al., H_2 Ti_6 O_{13} Nanosheet/ Polymethyl Methacrylate (PMMA) for the adsorption of cesium ions. J. Solid. State. Chem. **324**, 124047 (2023). https://doi.org/10.1016/j.jssc.2023.124047
8. H. Bayadsi, P.V. Brink, M. Erlandsson et al., The correlation between small papillary thyroid cancers and gamma radionuclides Cs-137, Th-232, U-238 and K-40 using spatially-explicit, register-based methods. Spat. Spatio-Temporal. **47**, 100618 (2023). https://doi.org/10.1016/j.sste.2023.100618
9. T. Hong, Y. Pan, Y. Liu et al., The mechanism and behavior of cesium adsorption from aqueous solutions onto carbonated cement slurry powder. J. Environ. Radioactiv. **272**, 107350 (2024). https://doi.org/10.1016/j.jenvrad.2023.107350
10. H. Wu, T. Kudo, S.Y. Kim et al., Recovery of cesium ions from seawater using a porous silica-based ionic liquid impregnated adsorbent. Nucl. Eng. Technol. **54**, 1597–1605 (2022). https://doi.org/10.1016/j.net.2021.10.026
11. Z. Chen, Y. Wu, Y.Z. Wei, The effect of temperatures and γ-ray irradiationon silica-based calix[4]arene-R14 adsorben tmodified with surfactants for the adsorption of cesium from nuclear waste solution. Radiat. Phys. Chem. **103**, 222–226 (2014). https://doi.org/10.1016/j.radphyschem.2014.06.004
12. X.X. Zhang, Y. Wu, Y.Z. Wei et al., Stable solidification of cesium with an allophane additive by a pressing/sintering method. J. Nucl. Mater. **485**, 39–46 (2017). https://doi.org/10.1016/j.jnucmat.2016.12.029
13. J.L. Wang, S.T. Zhuang, Cesium separation from radioactive waste by extraction and adsorption based on crown ethers and calixarenes. Nucl. Eng. Technol. **52**, 328–336 (2020). https://doi.org/10.1016/j.net.2019.08.001
14. W.A. Li, Y.C. Peng, W. Ma et al., Rapid and selective removal of Cs^+ and Sr^{2+} ions by two zeolite-type sulfides via ion exchange method. Chem. Eng. J. **442**, 136377 (2022). https://doi.org/10.1016/j.cej.2022.136377
15. S.Q. Chen, X.N. Yang, Z. Wang et al., Prussian blue analogs-based layered double hydroxides for highly efficient Cs^+ removal from wastewater. J. Hazard. Mater. **410**, 124608 (2021). https://doi.org/10.1016/j.jhazmat.2020.124608
16. N.D. Trung, N. Ping, L.T.H. Lan et al., Synthesis, characterization, and caesium adsorbent application of trigonal zinc hexacyanoferrate (II) nanoparticles. J. Environ. Chem. Eng. **9**, 106772 (2021). https://doi.org/10.1016/j.jece.2021.106772
17. F.L. Song, X.W. Yang, X.L. Li et al., The behavior of cesium adsorption on zirconyl pyrophosphate. Nucl. Sci. Tech. **27**, 60 (2016). https://doi.org/10.1007/s41365-016-0054-1
18. H. Mimura, Y. Wu, Y. Wang et al., Selective separation and recovery of cesium by ammonium tungstophosphate-alginate

microcapsules. Nucl. Eng. Des. **241**, 4750–4757 (2011). https://doi.org/10.1016/j.nucengdes.2011.03.031
19. H. Dan, Q. Xian, L. Chen et al., One-step direct synthesis of mesoporous AMP/SBA-15 using PMA as acid media and its use in cesium ion removal. J. Nucl. Mater. **527**, 151809 (2019). https://doi.org/10.1016/j.jnucmat.2019.151809
20. Y. Wang, K. Li, D. Fang et al., Ammonium molybdophosphate/metal-organic framework composite as an effective adsorbent for capture of Rb+ and Cs+ from aqueous solution. J. Solid. State. Chem. **306**, 122767 (2022). https://doi.org/10.1016/j.jssc.2021.122767
21. I. Malakhova, Y. Parotkina, M. Palamarchuk et al., Composite Zn(II) ferrocyanide/polyethylenimine cryogels for point-of-use selective removal of Cs-137 radionuclides. Molecules. **26**, 4604 (2021). https://doi.org/10.3390/molecules26154604
22. M. Kim, S. Eun, J. Ryu et al., Efficient removal of Cs ion by electrochemical adsorption and desorption reaction using NiFe Prussian blue deposited carbon nanofiber electrode. J. Hazard. Mater. **443**, 130215 (2023). https://doi.org/10.1016/j.jhazmat.2022.130215
23. S. Chitra, A.G. Shanmugamani, R. Sudha et al., Selective removal of cesium and strontium by crystalline silicotitanates. J. Radioanal. Nucl. Ch. **312**, 507–515 (2017). https://doi.org/10.1007/s10967-017-5249-3
24. J.H. Tang, M.L. Feng, X.Y. Huang, Metal chalcogenides as ion-exchange materials for the efficient removal of key radionuclides: a review. Fundamental Research (2024). https://doi.org/10.1016/j.fmre.2023.10.022
25. K. Suresh, M.S. Babu, P. Jagasi, Zirconium based metal-organic framework as highly efficient and acid-stable adsorbent for the rapid removal from of Sr^{2+} and Cs^{+} solution. Sep. Purif. Technol. **335**, 126052 (2024). https://doi.org/10.1016/j.seppur.2023.126052
26. S.S. Emmanuel, C.O. Olawoyin, A.A. Adesibikan et al., Solvothermally and non-solvthermally fabricated covalent organic frameworks (COFs) for eco-friendly remediation of radiocontaminants in aquatic environments: A review. J. Organomet. Chem. **1005**, 122984 (2024). https://doi.org/10.1016/j.jorganchem.2023.122984
27. Y. Wu, X.X. Zhang, Y.Z. Wei et al., Development of adsorption and solidification process for decontamination of Cs-contaminated radioactive water in Fukushima through silica-based AMP hybrid adsorbent. Sep. Purif. Technol. **181**, 76–84 (2017). https://doi.org/10.1016/j.seppur.2017.03.019
28. A.F. Holdsworth, H. Eccles, D. Rowbotham et al., The effect of gamma irradiation on the physiochemical properties of Caesium-Selective ammonium phosphomolybdate-polyacrylonitrile (AMP-PAN) composites. Clean Technol. **1**, 20 (2019). https://doi.org/10.3390/cleantechnol1010020
29. J.J. Yang, J.K. Wang, J.P. Guo et al., Dendrimer modified composite magnetic nano-flocculant for efficient removal of graphene oxide. Sep. Purif. Technol. **307**, 122851 (2023). https://doi.org/10.1016/j.seppur.2022.122851
30. R. Chakraborty, S. Dhara, S. Basu et al., Quinolinephosphomolybdate as ion exchanger: synthesis, characterization, and application in separation of ^{90} Y from ^{90} Sr. J. Radioanal. Nucl. Ch. **287**, 55–59 (2011). https://doi.org/10.1007/s10967-010-0688-0
31. R. Chakraborty, K. Bhattacharaya, P. Chattopadhyay, Nanostructured zirconium phosphate as ion exchanger: synthesis, size dependent property and analytical application in radiochemical separation. Appl. Radiat. Isotopes. **85**, 34–38 (2014). https://doi.org/10.1016/j.apradiso.2013.10.018
32. R. Chakraborty, S. Chatterjee, P. Chattopadhyay, Radioanalytical separation and size-dependent ion exchange property of micelle-directed titanium phosphate nanocomposites. J. Radioanal. Nucl. Ch. **299**, 1565–1570 (2014). https://doi.org/10.1007/s10967-013-2815-1
33. T. Yousefi, A.R. Khanchi, S.J. Ahmadi et al., Cerium(III) molybdate nanoparticles: Synthesis, characterization and radionuclides adsorption studies. J. Hazard. Mater. **215–216**, 266–271 (2012). https://doi.org/10.1016/j.jhazmat.2012.02.064
34. P. Pegallapati, M. Reddivari, B. Pejjai et al., Synthesis of Cu-doped ZnS nano-powder by chemical co-precipitation process. Mater. Today-Proc. (2023). https://doi.org/10.1016/j.matpr.2023.02.419
35. Q. Wang, F. Du, Y.K. Hou et al., Preparation of a CeO_2-ZrO_2 based nano-composite with enhanced thermal stability by a novel chelating precipitation method. Ceram. Int. **47**, 33057–33063 (2021). https://doi.org/10.1016/j.ceramint.2021.08.206
36. H. Wu, L.Q. Chen, C. Tang et al., Silver nanoparticles catalyzed electrochemical hydrodechlorination of dichloromethane to methane in N, N-Dimethylformamide using water as hydrogen donor. Sep. Purif. Technol. **331**, 125647 (2024). https://doi.org/10.1016/j.seppur.2023.125647
37. X. Xie, X. Tang, L. Yan et al., Morphological and microstructural evolutions of chemical vapor reaction-fabricated SiC under argon ion irradiation. Nucl. Instrum. Meth. B. **541**, 151–160 (2023). https://doi.org/10.1016/j.nimb.2023.05.066
38. Z.H. Zhang, S.D. Zhang, C.J. Jiang et al., Integrated sensing array of the perovskite-type $LnFeO_3$ (Ln=La, Pr, Nd, Sm) to discriminate detection of volatile sulfur compounds. J. Hazard. Mater. **413**, 125380 (2021). https://doi.org/10.1016/j.jhazmat.2021.125380
39. T. Yousefi, S. Yavarpour, S.H. Mousavi et al., $FeIII_x$ $SnII_y$ $SnIV_{1-x-y}$ $H_n[P(Mo_3O_{10})_4] \cdot xH_2O$ new nano hybrid, for effective removal of Sr(II) and Th(IV). J. Radioanal. Nucl. Chem. **307**, 941–953 (2016). https://doi.org/10.1007/s10967-015-4295-y
40. K. Shi, C.L. Zhao, Z.R. Liu, Studies on the co-polymerization of Sn and Fe solutions. CIESC J. **50**, 262–266 (1999). https://doi.org/10.3321/j.issn:0438-1157.1999.02.017
41. Y. Tan, Y. Wang, H. Liu et al., Synthesis and high-temperature phase transformation behavior of Dy_2O_3-Sc_2O_3 co-stabilized ZrO_2 powders prepared by cocurrent chemical coprecipitation. Ceram. Int. **50**, 22395–22404 (2024). https://doi.org/10.1016/j.ceramint.2024.03.340
42. J.C.A. Boeyens, G.J. McDougal, J. Van, R. Smit, Crystallographic study of the ammonium/potassium 12-molybdophosphate ion-exchange system. J. Solid. State. Chem. **18**, 191–199 (1976). https://doi.org/10.1016/0022-4596(76)90095-5
43. Q.L. Wang, H.J. Sang, L.F. Chen et al., Selective separation of Pd(II) through ion exchange and oxidation-reduction with hexacyanoferrates from high-level liquid waste. Sep. Purif. Technol. **231**, 115932 (2020). https://doi.org/10.1016/j.seppur.2019.115932
44. T. Yousefi, A.N. Golikand, M.H. Mashhadizadeha et al., Template-free synthesis of MnO_2 nanowires with secondary flower like structure: characterization and supercapacitor behavior studies. Curr. Appl. Phys. **12**, 193–198 (2012). https://doi.org/10.1016/j.cap.2011.05.038
45. H. Tian, X. Huang, B. Zhao et al., Investigation of the mechanism and interaction of nitrogen conversion during lignin/glutamic acid co-pyrolysis. J. Anal. Appl. Pyrol. **183**, 106795 (2024). https://doi.org/10.1016/j.jaap.2024.106795
46. N.R. Azeez, S.S. Salih, M. Kadhom et al., Enhanced termination of zinc and cadmium ions from wastewater employing plain and chitosan-modified mxenes: synthesis, characterization, and adsorption performance. Green. Ch. E. **5**, 339–347 (2024). https://doi.org/10.1016/j.gce.2023.08.003
47. M. Kosmulski, The pH dependent surface charging and points of zero charge. X. Update. Adv. Colloid. Interfac. **5**, 339–347 (2024). https://doi.org/10.1016/j.gce.2023.08.003
48. M.R. Awual, S. Suzuki, T. Taguchi et al., Radioactive cesium removal from nuclear wastewater by novel inorganic and

conjugate adsorbents. Chem. Eng. J. **242**, 127–135 (2014). https://doi.org/10.1016/j.cej.2013.12.072
49. S.S. Salih, M. Kadhom, M.A. Shihab et al., Competitive adsorption of Pb(II) and phenol onto modified chitosan/vermiculite adsorbents. J. Polym. Environ. **30**, 4238–4251 (2022). https://doi.org/10.1007/s10924-022-02515-0
50. S.S. Salih, M.A. Shihab, H.N. Mohammed et al., Chitosan-vermiculite composite adsorbent: preparation, characterization, and competitive adsorption of Cu(II) and Cd(II) ions. J. Water Process. Eng. **59**, 105044 (2024). https://doi.org/10.1016/j.jwpe.2024.105044
51. J. Wang, X. Guo, Adsorption isotherm models: classification, physical meaning, application and solving method. Chemosphere. **258**, 127279 (2020). https://doi.org/10.1016/j.chemosphere.2020.127279
52. Y.Q. Wang, Y.Y. Wen, C. Mao et al., Development of chromatographic process for the dynamic separation of ^{90}Sr from high level liquid waste through breakthrough curve simulation and thermal analysis. Sep. Purif. Technol. **282**, 120103 (2022). https://doi.org/10.1016/j.seppur.2021.120103
53. C. Liu, W. Wang, N. Wang et al., Synthesis of cubic mesoporous silica SBA16 functionalized with carboxylic acid in a one-pot process for efficient removal of wastewater containing Cu_2^+: Adsorption isotherms, kinetics, and thermodynamics. Micropor. Mesopor. Mat. **382**, 113402 (2024). https://doi.org/10.1016/j.micromeso.2024.113402
54. Y. Ding, R. He, C. Wang et al., Efficient separation of Cd^{2+} and Pb^{2+} by Tetradesmus obliquus: insights from cultivation conditions with competitive adsorption modeling. J. Water Process. Eng. **60**, 105207 (2024). https://doi.org/10.1016/j.jwpe.2024.105207
55. J. Wang, X. Guo, Rethinking of the intraparticle diffusion adsorption kinetics model: interpretation, solving methods and applications. Chemosphere **309**, 136732 (2022). https://doi.org/10.1016/j.chemosphere.2022.136732
56. Z. Wang, R. Miao, P. Ning et al., From wastes to functions: A paper mill sludge-based calcium-containing porous biochar adsorbent for phosphorus removal. J. Colloid. Interf. Sci. **593**, 434–446 (2021). https://doi.org/10.1016/j.jcis.2021.02.118
57. S. Zhuo, T. Dai, H. Ren et al., Simultaneous adsorption of phosphate and tetracycline by calcium modified corn stover biochar: performance and mechanism. Bioresource Technology. **359**, 127477 (2022). https://doi.org/10.1016/j.biortech.2022.127477
58. H.J. Sang, C. Mao, F.C. Ming et al., Selective separation and immobilization process of ^{137}Cs from high-level liquid waste based on silicon-based heteropoly salt and natural minerals. Chem. Eng. J. **449**, 137842 (2022). https://doi.org/10.1016/j.cej.2022.137842